Citation (APA)
Pot, H., Christiaens, B., Wellens, P., Schreier, S., & Westerweel, J. (2026). Assessing large hydroelastic parameter spaces through a table-top Faraday experiment. In T. Kristiansen, M. Greco, & D. Kristiansen (Eds.), *Proceedings of the 10th International Conference on HYDROELASTICITY IN MARINE TECHNOLOGY* (pp. 339-348). NTNU.

Assessing large hydroelastic parameter spaces through a table-top Faraday experiment

H. Pot[1,*] B. Christiaens[2,*] P. Wellens[1,*] S. Schreier[1,*] J. Westerweel[2]

[1] Department of Maritime and Transport Technology, Delft University of Technology, Delft, The Netherlands
[2] Laboratory of Aero and Hydrodynamics, Delft University of Technology, Delft, The Netherlands

Abstract. This study investigates the influence of stiffness on the hydroelastic wave-structure interactions of floating sheets, a concept for offshore photovoltaics. We propose an experimental method in which we can vary models, amplitudes and frequencies effortless, since conventional experimental methods have limitations, especially for large out-of-plane deformations. Moreover, green water effects which often occur for steep waves are eliminated with this setup. This study investigates the applicability of linear hydroelastic theory with the measurements on two floating membranes with different thickness. The measured hydroelastic wavelengths are for both membranes larger than the predictions by the theoretical hydroelastic dispersion. We find that the measurements of both thicknesses can be matched if an in-plane tension is added to the linear hydroelastic dispersion relation. This study demonstrates that the measurements are not well predicted by the linear theory and the stresses in the structure are most likely underestimated by this prediction.

Key words: *Fluid-structure interactions; Hydroelastic dispersion; Floating membrane; Experiments, Synthetic Schlieren*

1. Introduction

Certain offshore structures evolve into increasingly flexible designs with vast principal dimensions. Such designs include floating airports [16], flexible breakwaters [17], wave energy converters [18, 19] and floating solar [20, 12, 21]. The latter may be most economically beneficial when it covers large spatial domains, and when investment cost are minimized by using a flexible floater design [22]. Flexible designs in offshore waves environments may be prone to out-of-plane deflections much larger than their own thickness [23]. This may induce loads beyond the often used linear approximations.

Figure 1 shows an often used characterisation for large floating structures such as floating airports, sea ice, and floating solar [16, 23]. This logarithmic figure stresses the vast range of scales associated with these designs: there are large variations in structure lengths, in hydroelastic stiffness (characteristic length), and the ratio between the structure length and the wavelength. Most numerical models are limited to linear plate theory [23]. However, the magnitude of the out-of-plane deformations is often not within the intended range of the linear plate theory and linear approximations most likely underestimates the strains in the structure [24, 23, 25]. Including geometrically nonlinear strains could therefore improve the load predictions. This however requires advanced modeling approaches.

In experimental research, the large surface coverage poses challenges since common facilities such as towing tanks have limited widths. Therefore, blocking effects or reflections can affect the response [26]. Therefore, large and expensive basins are generally necessary if scaling of the principal dimensions is required [27, 28, 4]. Secondly, often only a narrow parameter space and a single or a few models are tested, since exchanging models is labor intensive [27, 12, 29, 1, 4]. Experimental attempts in steep

*Correspondence to: h.m.pot@tudelft.nl

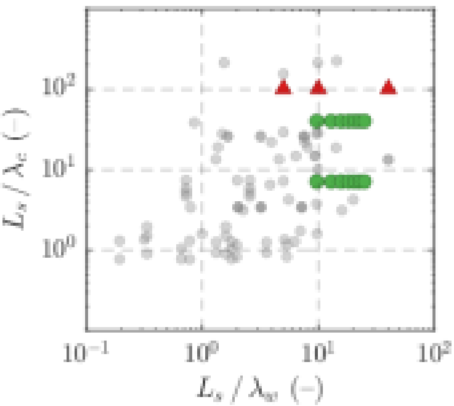

Figure 1: Typical characterisation of large floating structures, with experimental measurements reported in other studies (grey ∘), the measurements of the current study (green ∘), and the foreseen real scale application (red △). The literature data includes experimental studies to sea ice [1, 2, 3, 4, 5, 6, 7, 8, 9], Very Large Floating Structure (VLFS) [10, 11], floating PV [12], and small scale ($L_{basin} < 1$ m) floating membranes experiments [13, 14, 15]. The characteristic length is defined as a relation between the bending rigidity D and the hydrostatic stiffness ρg, $\lambda_c = (\frac{D}{\rho g})^{1/4}$.

waves report challenges regarding green water [29]. Moreover, when the models are delicate membranes, direct strain measurements are often difficult to perform, since strain gauges may be stiffer that the model itself, and optical strain measurements are not always possible due to large model motions. The typical foreseen non-dimensional parameters for the real scale application of floating solar are presented by the red triangles in Figure 1. Almost no experimental systematic variations of the stiffness are performed in this region. The proposed systematic variations are however necessary to understand the loads in the structure, especially for significant wave amplitudes.

In sea ice predictions and large scale floating membranes one-dimensional dispersion relations are often used to predict the hydroelastic wave-structure interaction [7, 30, 31, 32, 8]. When the planar dimensions increase, the hydroelastic deformations are the dominant response [33]. Therefore, hydroelastic dispersion relations may be suitable to model the response of a large floating sheet in waves. Hydroelastic dispersion relations can yield various load contributions, including mass, bending rigidity, pretension and gravity. Therefore it may be possible to study the relative contribution of different load terms by fitting the dispersion relation to measured responses. In experimental small-scale studies, the hydroelastic waves are well described by linear dispersion relations [31, 13, 14]. In analytical studies, nonlinear steepness is often added via perturbations. Such studies are however rarely validated with experimental data. Therefore, it is not certain if and how nonlinearities in the structure appear, and whether or not that is correctly modeled by the analytical approaches.

In this study, we propose a table-top experimental method to study the loads within a membrane under wave loading. A Faraday experiment is employed in which a small basin is vertically excited by a shaker through which standing waves are generated. The setup allows for a large parameter space to be explored, as illustrated in Figure 1. We compare the measurements with linear hydroelastic dispersion relations, since these are used to study the governing loads in the structure and to relate the small scale findings to real scale application size. Also, we aim to obtain insights in the response variations when the deformation amplitude increases.

2. Theory

2.1. Faraday Waves

Faraday waves are standing waves excited by a vertical vibration of the basin. The surface deformation ζ of the medium can be described by a Mathieu equation. In ship hydrodynamics, this equation is used to describe parametric roll. For an ideal fluid with phenomenological damping, this equation reads [34]:

$$\ddot{\zeta} + 2\gamma\dot{\zeta} + \omega[1 - \hat{a}\cos(\omega_e t)]\zeta = 0, \tag{1}$$

with ω_e the oscillating frequency of the shaker, ω the wave frequency, and $\hat{a}$ the non-dimensional amplitude of the shaker. Likewise the onset of parametric roll, the onset of Faraday waves starts when the energy inserted in the system by the shaker exceeds the viscous damping. The onset follows so-called stability tongues, with its minima occurring at $\omega_e/\omega = 2/n$ for n = 1, 2, 3, ... The lowest harmoninic response thus occurs at the subharmonic frequency $\omega = \omega_e/2$.

The relation between the sub-harmonic wave frequency and the wavelength is for fluids well described by the dispersion relation. An important note hereby is, that right after the onset amplitude of the waves, the geometry of the basin demands the wave patterns. For a circular basin, this results in a circular wave pattern which looks like Bessel functions. Above the onset amplitude, the pattern is indifferent of geometry of the basin [35]. Therefore the same wave patterns can be generated in for instance circular or square basins. In this study we focus on wave patterns independent of geometry of the basin.

2.2. Dispersion relations

The dispersion relation for water waves yields [36]:

$$\omega^2 = \left(g + \frac{\sigma}{\rho}k^2\right) k \tanh kd, \tag{2}$$

and describes the fixed relation between the wave frequency ω and wave number k through the gravitational acceleration g, the surface tension σ, the density of the fluid ρ, and the water depth d. Now, we assume a free floating thin plate with thickness h, structural mass per unit area $\rho_s h$, and bending rigidity $D = \frac{Eh^3}{12(1-\nu^2)}$, with Young's Modulus E, and Poisson ratio ν. With the classical thin plate theory, the governing equation becomes [32]:

$$D\nabla^4\zeta - T\nabla^2\zeta + \rho_s h\zeta_{tt} = p, \tag{3}$$

with ζ the vertical sheet displacement, p the pressure acting on the bottom of the sheet imposed by the fluid, which is defined by the linearised Bernoulli equation, and ∇^2 and ∇^4 the Laplacian and bi-Laplacian operators, defined as $\nabla^2 = \frac{\partial^2}{\partial x^2} + \frac{\partial^2}{\partial y^2}$ and $\nabla^4 = \frac{\partial^4}{\partial x^4} + 2\,\frac{\partial^4}{\partial x^2 \partial y^2} + \frac{\partial^4}{\partial y^4}$, respectively. Here, T can be uniform and isotropic tension [14] or compression [32] in the sheet. We assess the limit in which the inertia of the sheet is much lower than the inertia of the fluid, and therefore neglect the sheet inertia. The dispersion relation is than derived as [32]:

$$\omega^2 = \left(g + \frac{T}{\rho}k^2 + \frac{D}{\rho}k^4\right) k \tanh kd. \tag{4}$$

In the limit where capillary effects are non-negligible, the air-water interface surface tension σ as presented in Eq. 2 is a component of T, acting as a dynamic, wave motion dependent tension. Therefore, T is defined as $\sigma + T_{add}$, with T_{add} being any other in-plane tension, if present. In the limit of a very small thickness compared to the wavelength, or the material being extremely flexible, the bending rigidity is negligible, through which the sheet is often referred to as membrane. In this limit, pretension is necessary to prevent the membrane from wrinkling or folding.

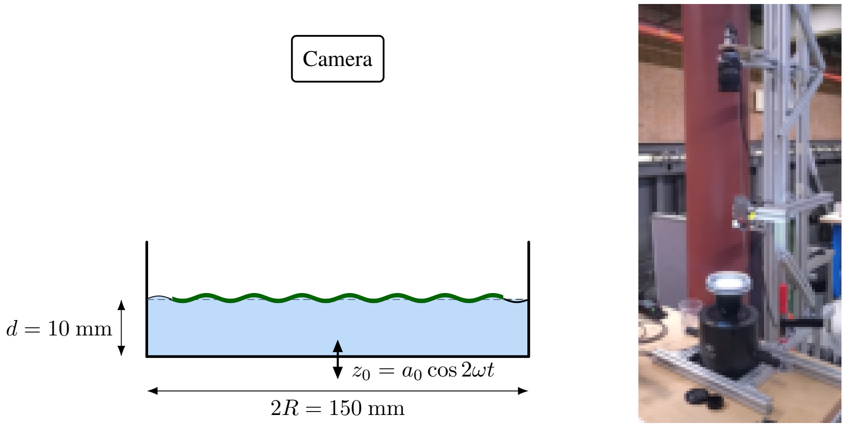

Figure 2: Experimental setup with an oscillating basin, a thin floating sheet, and a camera positioned above the basin.

3. Methods

Measurements are performed in a vertically shaking fluid basin (Figure 2). The fluid basin is a cylindrical container with a diameter of 150 mm. The shaker is a Brüel & Kjaer Vibration Exciter Type 4808, driven by a Brüel & Kjaer Power Amplifier Type 2719. The oscillations are controlled by a NF Electronic Instruments 1930A multifunction synthesizer. The fluid depth is 10 ± 0.8 mm. The ambient temperature of the laboratory and the fluid is 20 ± 2 °C.

A 2.3 MP Basler a2A1920-150μm camera (1920×1200 pixels) is mounted 800 mm above the tank. The exposure time is 2 ms, and the gain is 12. The lens is a Nikon Af-S NIKKOR 24-85 mm f/3.5-4.5G ED VR. A random dot pattern with a dot diameter of 0.25 mm on transparent paper is placed under the basin to perform optical correlation with *Synthetic Schlieren* [37]. To enhance the speckle contrast, a circular LED light of 70 mm diameter is positioned directly below the dot pattern. The shaker accelerations are measured with an accelerometer connected to the shaker, using a PCB Model 482B11 ICP signal conditioner (accuracy $\pm$ 1.6 %). The image acquisition is phase-locked using a frequency divider to minimize errors due to phase shifting. The camera is triggered by a TTL output from the shaker excitator. The acquisition rate is directly related to the shaker frequency and is approximately 4 Hz. Pylon viewer (Basler, Germany) is used for image acquisition.

Circular samples of transparent elastic films (ELASTOSIL Film 2030, Wacker Chemie AG) with diameters of 120 mm are free floating on the fluid, leaving an average space of 15 mm with the walls of the basin. The samples have a thickness of 20 ± 0.4 μm and 200 ± 4.0 μm, respectively, by manufacturer's statement. The material density is 1.075 ± 0.025 g/cm^3, and a Poisson ratio of 1/2 is assumed. The manufacturer's stress-strain test for small strains reports a Young's Modulus of 0.58 ± 0.02 MPa. With a static hydroelastic wrinkle test [38] this is verified as 0.6 ± 0.2 MPa. The characteristic length $\lambda_c = (\frac{D}{\rho g})^{1/4}$ is 0.48 mm and 2.7 mm for the thin and the thick sheet, respectively.

Demineralised water is used as a test fluid, which is refreshed at the start of each day to minimize contamination. During the experiments, the sheets remained in a stable position, without making contact with the side walls of the tank. Trapped air bubbles and water drops are carefully removed prior to testing. The shaker frequency is varied from 30 Hz to 90 Hz with steps of 10 Hz, resulting in a subharmonic response frequency of half the shaker frequency. For clarity, the subharmonic response frequency is used in the latter of this work. Six wave amplitudes are tested at each frequency. Figure 3 shows the measured response heights and steepness per frequency.

Prior to each test a reference image is acquired. The displacement fields of 100 images are com-

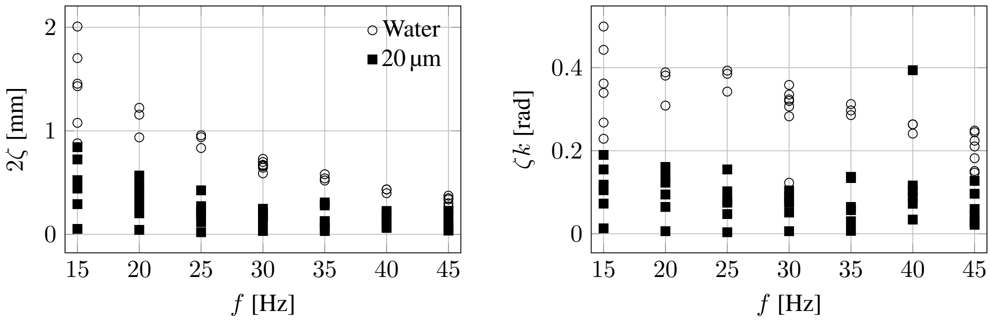

(a) Measured deformation amplitudes per frequency.

(b) Measured deformation steepness per frequency.

Figure 3: (a) Measured amplitudes (b) steepness for water waves and the floating membrane of thickness h = 20μm. The classic thin plate assumptions are considered valid for $\zeta k \leq 0.1$, with $0.1 < \zeta k < 0.2$ a transition regime. For fluids, $\zeta k > 0.2$ is known as strongly nonlinear waves.

puted via cross-correlation with the reference image using commercial software (DaVis 11 Strainmaster, LaVision GmbH, Göttingen, Germany), and a window size of 25 $\times$ 25 px^2 and stepsize of 9 px (0.54 mm). The raw images and computed displacements are shown in Figure 4. The amplitude fields are reconstructed from the displacement fields using the PIVMAT MATLAB library developed by [37]. Amplitude field analysis is performed with a 2D Fourier spectrum. Zero-padding is applied to improve peak localisation. Thereafter, the 2D spectrum is azimuthally averaged to obtain the 1D power spectrum. An average power spectrum is computed from all processed images of each test. The width of the dominant peak at 80% (arbitrarily chosen) of its maximum amplitude is used as an estimate of the wavelength uncertainty.

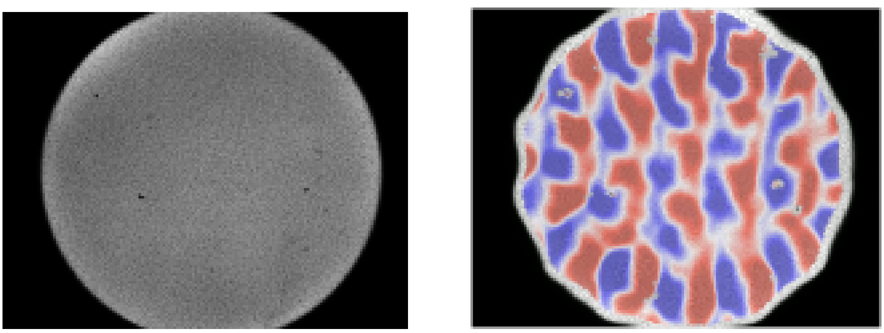

(a) Raw camera image.

(b) Displacement field.

Figure 4: (a) Raw camera image at still water and (b) DIC displacement field computed by cross-correlation in DAVIS. Note that these do not represent the actual deformation amplitudes, which are subsequently computed in MATLAB using the refractive method *Synthetic Schlieren*.

4. Results

Figure 5 shows the instantaneous hydroelastic deformation fields for h = 20 μm at wave frequencies of 15 Hz and 45 Hz, respectively. Note that the shaker frequency here is 30 Hz and 90 Hz, respectively,

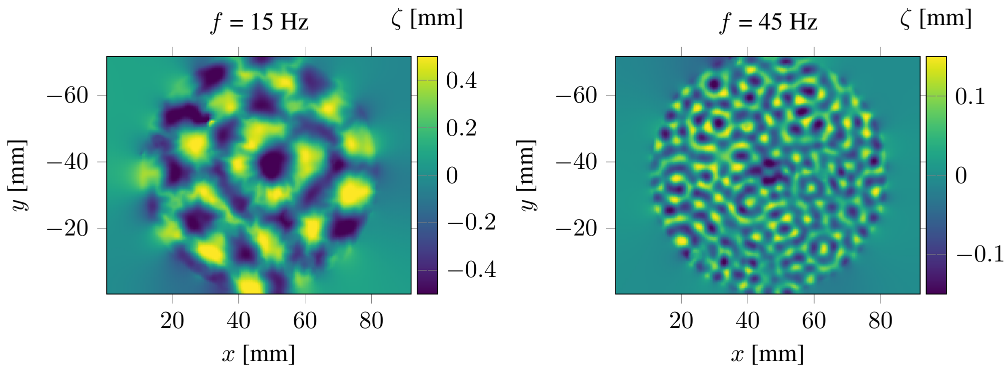

Figure 5: Instantaneous deformation field $\zeta(x, y)$ for the h = 20 μm membrane at (a) f = 15 Hz and (b) f = 45 Hz.

and that the wave frequency is subharmonic with respect to the shaker frequency (see Eq. 1). The Figure shows that the hydroelatic standing waves appear with a distinctive wavelength. The orientation of the waves is not influenced by the circular edges of the basin. The basin edges only have an effect when the shaker frequency is close to the natural frequency of the basin and the fluid, or when the wave amplitude is just above onset amplitude [35]. Above these thresholds, the waves are omnidirectional and the wavelengths are, for bare fluids, governed by dispersion relations [39].

Figure 6 shows the measured wavelengths over the range of frequencies for water and floating sheets of h = 20 μm and h = 200 μm. The effective surface tension of the air-water interface is computed by fitting Eq. 2 to the measurements with bare water, with σ = with 28 mN/m. This fitted surface tension is significantly lower than the theoretical value of 72 mN/m. However, contamination of water is well known to drastically decrease the surface tension, and various studies report similar values [40, 31, 39].

Figure 6 shows that the theoretical dispersion relation (red dotted line) for h = 20 μm is nearly identical to the dispersion relation of water. Here, the magnitude of the bending rigidity D of Eq. 4 is very small due to the thinness of the membrane. The measured wavelength for h = 20 μm are however slightly larger than this theoretical relation. Since the bending rigidity is near zero, this effect is more likely explained by an additional tension term. Indeed, if a tension term scaling to $\sim k^3$ of T_{add} is added to the theoretical dispersion relation, all measurement data of smallest steepness bin of h = 20 μm ly on the dispersion curve. $T_{add} = 10$ mN/m fits best for this thickness.

A possible explanation for this may be the presence of a uniform pre-tension as a result of the surface tension. A graphical explanation of this is shown in Figure 7. Due to the capillary effect of the fluid, the surface tension may impose a static pulling force on the edges of the membrane, a phenomena also observed at the edges of vertical walls [41]. Since this occurs along the circumference of the membrane, the effect may impose a uniform pretension. We test this hypotheses by drastically decreasing the surface tension by adding a surfactant (soap) when the membrane is at rest. In that case, the membrane shows wrinkles and folds and is not able to form a flat floating layer. We therefore conclude that some effect of static pre-tension is acting on the edges of the membrane caused by the surface tension. Note that the *dynamic* surface tension as included in Eq. 2 is also still present in the force balance, but only in dynamic conditions as it is curvature dependent. The interested reader is referred to [41] in which a thorough explanation of this concept is found. However, in-plane tensions from other sources also lead to longer wavelengths. They can originate from the nonlinear membrane effect (vón Kármàn strains). Note that in the current setup we cannot differentiate between the relative influence of the two in-plane tensions.

The measured wavelengths for h = 200 μm are significantly longer than for h = 20 μm. The theoretical dispersion relation for h = 200 μm (dash-dotted line) predicts significantly longer wavelengths

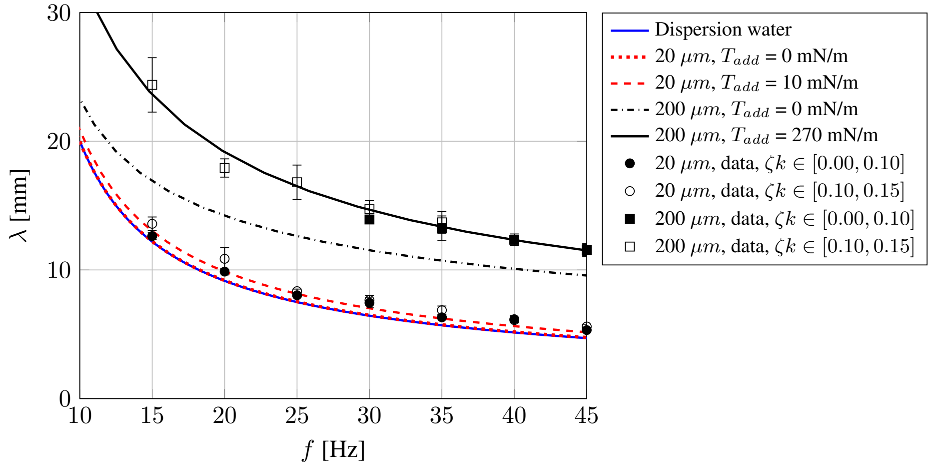

Figure 6: Theoretical dispersion relations (Eq. 4) and the measured data for h = 20 μm and h = 200 μm. The data is binned by steepness. The filled markers indicate a steepness range $\zeta k \in [0.00, 0.10]$, while the open markers indicate a steepness range $\zeta k \in [0.10, 0.15]$. The theoretical dispersion relations for h = 20 μm and h = 200 μm are displayed by the red dotted line and the black dash-dotted line, respectively. The red dashed line is fitted to the data of the lowest steepness bin of h = 20 μm by adding T_{add} = 10 mN/m to Eq. 4, and the black solid line to the data in the lowest bin of h = 200 μm with T_{add} = 270 mN/m. The data of both thicknesses is well described by the dispersion relations with the additional tension term. The dispersion relation for water with $\sigma = 28$ mN/m is shown in blue.

Figure 7: Capillary effect the fluid acting on the edges of the membrane. The angle of the capillary arc influences the magnitude of the horizontally applied tension to the membrane [41].

than the theoretical dispersion relation for h = 20 μm does (dotted line). This indicates the significant theoretical influence of the bending rigidity. The theoretical curve however largely under-predicts the measured wavelengths, and indicates that additional stresses are present under the loading. We therefore add a tension of T_{add} = 270 mN/m to Eq. 4 which closely fits all measurement data, likewise the addition of $T_{add} = 10$ mN/m for h = 20 μm. The wavelengths of both thicknesses can be accurately described by the theoretical dispersion relation including an additional tension term which scales with $\sim k^3$ in the dispersion relation. Therefore we assume that a different stress-strain relation may be more applicable for the membranes.

In Figure 6 the individual measurements are binned per response steepness ζk, where the filled markers indicate a steepness range $\zeta k \in [0.00, 0.10]$ and the open markers indicate a steepness range $\zeta k \in [0.10, 0.15]$. Despite uncertainties in the wavelengths, a larger wavelength is generally found for measurements with larger steepness. This may indicate that the steepness of current measurements already exceed the linear regime in which the dispersion relation of Eq. 4 is valid.

Figure 8a shows that the deformation amplitude linearly increases with the oscillation acceleration. Higher frequencies require a larger acceleration magnitude for similar size deformation amplitudes. The data also shows that a trend line would not pass through (0,0), indicating the presence of a typical Faraday experiment characteristic: the viscous threshold before waves start appearing at the surface. Figure

8b shows the measured wavelength against $2\zeta\, \ddot{a}_0^{-1}\, g$, which collapses the measurements of different frequencies. The frequencies are sorted by the same markers as in Figure 8a. For h = 20 μm, this results in a nearly straight line with narrow bandwidth. For a few frequencies, clearly different wavelengths are measured. This indicates the presence of nonlinear effects in the amplitude. The amplitude dependent effects are clearly non included in the linear dispersion relation of Eq. 4, clearly indicating the limitations for the current measurements. The 200 μm membrane shows a much larger spread in the wavelengths. The differences between both thicknesses indicate thickness-dependent nonlinear effects which may be a result of additional stress-strain relations in the thicker membrane or the Poisson penalty.

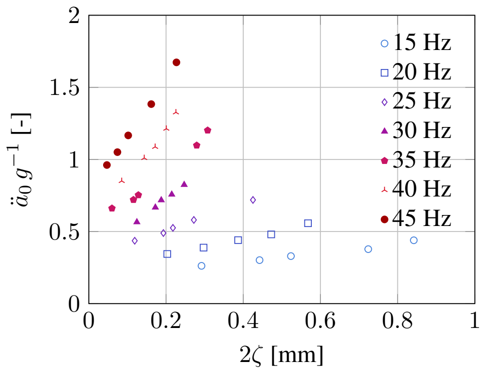

(a) Shaker accelerations against the deformation amplitude for $t = 20$ μm.

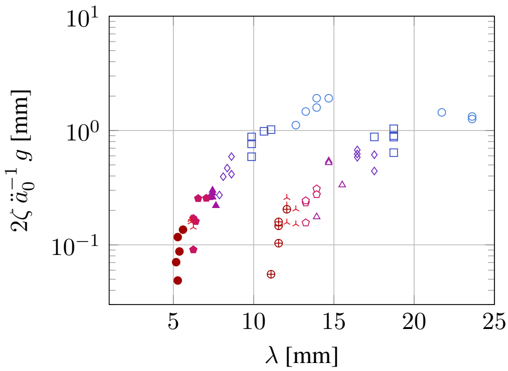

(b) Deformation amplitude over shaker acceleration against the wavelength.

Figure 8: Dynamic response of the membrane relative to the shaker acceleration. (a) The shaker accelerations against the deformation amplitude for h = 20 μm. The different frequencies are marked by colors ranging from blue (lowest frequencies) to red (highest frequencies) and are in detail shown in the legend. (b) The deformation amplitude over shaker acceleration against the wavelength. The same color- and marker scheme is used as in (a). The left data cloud is for h = 20 μm and the right data cloud for h = 200 μm.

5. Conclusions

This study shows that an additional tension in the linear hydroelastic dispersion relation is needed to predict the wavelengths in the floating membranes measured with the Faraday setup, which generates standing waves. For the thin membrane with $h = 20$ μm, the bending rigidity is insignificant compared to the gravitational loads, the surface tension and the additional tension. The measured wavelengths of the thin sheet are closely predicted by the linear dispersion relation, but the wavelengths of the thicker sheet are largely under-predicted by the linear dispersion relation. This observation disagrees with similar sized unidirectional progressive wave experiments [31, 13], where the linear dispersion relation serves as an excellent prediction for the wavelengths. The hydroelastic wavelengths of both membranes are excellently predicted when an additional tension scaling to $\sim k^3$ is added to the linear dispersion relation. We therefore attribute the discrepancy with linear theory to the effect of nonlinear stress-strain relations (vón Kármàn strains), although a direct confirmation of this effect with strain measurements is not possible with the current setup. In the current small scale setup, systematic variation of frequencies, amplitudes and floating models could effortless be measured. Due to the standing waves, no green water entered the floating model, a common challenge when measuring steep waves. This makes the setup useful for systematic variations and measurements on steep waves.

Acknowledgments

This study was funded by the Dutch Research Council (NWO) under the Grant Number 19002 ('FlexFloat') in the Open Technology Program (OTP). The authors are grateful for the fruitful discussions with prof. Willem van de Water, and the technical support by S. Tokgöz, C. P. Poot, J G den Ouden, F J Sterk, P Taudin Chabot, and A Piras.

References

[1] M. Meylan, L. Bennetts, C. Cavaliere, A. Alberello, and A. Toffoli. Experimental and theoretical models of wave-induced flexure of a sea ice floe. *Phys. Fluids*, 27:041704, 2015.

[2] K. Iijima, C. Ma, A. Pambela, and T. Maeda. DIC measurement of deflection waves travelling along a thin flexural plate floating at water surface. *Ocean Eng.*, 266:113079, 12 2022.

[3] M. Meylan. *The behaviour of sea ice in ocean waves*. PhD thesis, University of Otago, New Zealand.

[4] F. Montiel, F. Bonnefoy, P. Ferrant, L. Bennetts, V. Squire, and P. Marsault. Hydroelastic response of floating elastic discs to regular waves part 1: wave basin experiments. *J. Fluid Mech.*, 723:604–628, 2013.

[5] A. Pambela, C. Ma, T. Maeda, and K. Iijima. Stokes wave traveling along a thin elastic plate floating at water surface. *J. Fluids Struct.*, 120:103919, 2023.

[6] S. Parra, D. Sree, D. Wang, E. Rogers, J. Lee, C. Collins, A. Law, and A. Babanin. Experimental study on surface wave modifications by different ice covers. *Cold Regions Sci. Technol.*, 174:103042, 6 2020.

[7] S. Sakai and K. Hanai. Empirical formula of dispersion relation of waves in sea ice. In *Ice in the Environment: Proc. 16th IAHR Intern. Symp. on Ice*, pages 2–6. Intern. Assoc. Hydraulic Eng. Research, 12 2002.

[8] D. Sree, A. Law, and H. Shen. An experimental study on the interactions between surface waves and floating viscoelastic covers. *Wave Motion*, 70:195–208, 2017.

[9] D. Sree, A. Law, and H. Shen. An experimental study on gravity waves through a floating viscoelastic cover. *Cold Regions Sci. Technol.*, 155:289–299, 2018.

[10] H. Kagemoto, M. Fujino, and M. Murai. Theoretical and experimental predictions of the hydroelastic response of a very large floating structure in waves. *Appl. Ocean Res.*, 20:135–144, 1998.

[11] S. Schreier and G. Jacobi. Experimental investigation of wave interaction with a thin floating sheet. *Int. J. Offshore Polar Eng.*, 31(4):435–444, 2021.

[12] T. Kristiansen, P. Gron, and O. Faltinsen. A floating membrane solar island study. *Proc. 9th Int. Conf. Hydroelasticity Mar. Technol.*, pages 445–454, 2022.

[13] L. Domino, M. Fermigier, E. Fort, and A. Eddi. Dispersion-free control of hydroelastic waves down to sub-wavelength scale. *Eur. Phys. Lett.*, 121(1):14001, 2018.

[14] L. Deike, J. Bacri, and E. Falcon. Nonlinear waves on the surface of a fluid covered by an elastic sheet. *J. Fluid Mech.*, 733:394–413, 2013.

[15] L. Deike, M. Berhanu, and E. Falcon. Experimental observation of hydroelastic three-wave interactions. *Phys. Rev. Fluids*, 2:064803, 2017.

[16] H. Suzuki, B. Bhattacharya, M. Fujikubo, D. Hudson, H. Riggs, H. Seto, H. Shin, T. Shugar, Y. Yasuzawa, and Z. Zong. Very large floating structures. In *Proc. Int. Ship Offshore Struct. Congr.*, volume 2, pages 391–442, 2006.

[17] Y. Guo, S. Mohapatra, and C. Soares. Review of developments in porous membranes and net-type structures for breakwaters and fish cages. *Ocean Eng.*, 200, 2020.

[18] J. Orphin, A. Fleming, and C. Algie. Physical scale model testing of a flexible membrane wave energy converter: videogrammetric analysis of membrane operation. *Int. J. Mar. Energy*, 20:135–150, 2017.

[19] Y. Ye, J. Gan, H. Liu, W. Wu, S. Wang, and C. Soares. *A review of developments, material and mechanics of floating inflatable membrane structures for marine applications*, pages 649–657. CRC Press, 1 edition, 4 2025.

[20] S. Agarwal, O. Colomés, and A. Metrikine. Dynamic analysis of viscoelastic floating membranes using monolithic finite element method. *J. Fluids Struct.*, 129:104167, 2024.

[21] S. Oliveira-Pinto and J. Stokkermans. Marine floating solar plants: an overview of potential, challenges and feasibility. *Proc. Inst. Civ. Eng. Marit. Eng.*, 173:120–135, 2020.

[22] K. Trapani, D. Millar, and H. Smith. Novel offshore application of photovoltaics in comparison to conventional marine renewable energy technologies. *Renew. Energy*, 50:879–888, 2013.

[23] M. Zhang and S. Schreier. Review of wave interaction with continuous flexible floating structures. *Ocean Eng.*, 264:112404, 2022.

[24] M. Zhang and S. Schreier. Application of modal expansion method to very flexible floating structures (VFFSs). In *International Ocean and Polar Engineering Conference*, 6 2022.

[25] X. Chen, J. Jensen, W. Cui, and S. Fu. Hydroelasticity of a floating plate in multidirectional waves 1. *Ocean Eng.*, 30:1997–2017, 2003.

[26] A. Tassin, V. Cognet, A. Eddi, and M. Fermigier. Very large floating structure (VLFS) interacting with water waves: large scale laboratory experiments and numerical modelling. In *The 39th International Workshop on Water Waves and Floating Bodies*, 4 2024.

[27] S. Michele, S. Zheng, F. Buriani, A. Borthwick, and D. Greaves. Floating hydroelastic circular plate in regular and irregular waves. *Eur. J. Mech. B Fluids*, 99:148–162, 2023.

[28] Y. Cheng, C. Ji, G. Zhai, and G. Oleg. Oblique wave-induced responses of a VLFS edged with a pair of inclined perforated plates. *China Ocean Eng.*, 32:14–25, 2018.

[29] H. Pot, J. Westerweel, and S. Schreier. Stereoscopic digital image correlation for hydroelastic waves of floating membranes. *Meas. Sci. Technol.*, 36, 12 2025.

[30] P. Xu and P. Wellens. Fully nonlinear hydroelastic modeling and analytic solution of large-scale floating photovoltaics in waves. *J. Fluids Struct.*, 109:103446, 2022.

[31] J. Ono-Dit-Biot, M. Trejo, E. Loukiantcheko, M. Lauch, Raphaél, K. Dalnoki-Veress, and T. Salez. Hydroelastic wake on a thin elastic sheet floating on water. *Phys. Rev. Fluids*, 4:014808, 2019.

[32] R. Schulkes, R. Hosking, and A. Sneyd. Waves due to a steadily moving source on a floating ice plate. Part 2. *J. Fluid Mech.*, 180:297–318, 1987.

[33] P. Xu and P. Wellens. Theoretical analysis of nonlinear fluid–structure interaction between large-scale polymer offshore floating photovoltaics and waves. *Ocean Eng.*, 249, 2022.

[34] K. Kumar and L. Tuckermant. Parametric instability of the interface between two fluids. *J. Fluid Mech.*, 279:49–68, 1994.

[35] W. Edwards and S. Fauve. Patterns and quasi-patterns in the Faraday experiment. *J. Fluid Mech.*, 278:123–148, 11 1994.

[36] H. Lamb. *Hydrodynamics*. Dover Publications, 6 edition, 1932.

[37] F. Moisy, M. Rabaud, and K. Salsac. A synthetic schlieren method for the measurement of the topography of a liquid interface. *Exp. Fluids*, 46(6):1021–1036, 2009.

[38] D. Vella, P. Aussillous, and L. Mahadevan. Elasticity of an interfacial particle raft. *Europhys. Lett.*, 68:212–218, 2004.

[39] S. Douady. Experimental study of the Faraday instability. *J. Fluid Mech.*, 221:383–409, 1990.

[40] A. Ponce-Torres and E. Vega. The effects of ambient impurities on the surface tension. *EPJ Web Conf.*, 114, 2016.

[41] D. Vella. *The Fluid Mechanics of Floating and Sinking*. PhD thesis, University of Cambridge, 8 2007.